Particuology 115 (2026) 192–201

Contents lists available at ScienceDirect

Particuology

journal homepage: www.elsevier.com/locate/partic

High-temperature coal gangue-based composites for sustainable thermal energy storage: Characterization and performance assessment

Lei Zhang[a], Chenxi Zhang[a,b,*], Zezhong Wang[a], Xingbo Zhao[a], Jing Shen[c], Dingrong Bai[a,**]

[a] Ordos Laboratory, Ordos, Inner Mongolia, 017010, China
[b] Beijing Key Laboratory of Green Chemical Reaction Engineering and Technology, Department of Chemical Engineering, Tsinghua University, Beijing, 100084, China
[c] YanKuang Energy Group Company Limited, Zoucheng, 273500, China

HIGHLIGHTS

- Coal gangue can be converted into a sensible heat storage material.
- TES can be made cost-effective using coal-gangue-based materials.
- In-depth characterization relates the TES performance to the material properties.
- Coal gangue TES material reaches 555 kWh/m^3 of energy storage density at 1200 °C.

GRAPHICAL ABSTRACT

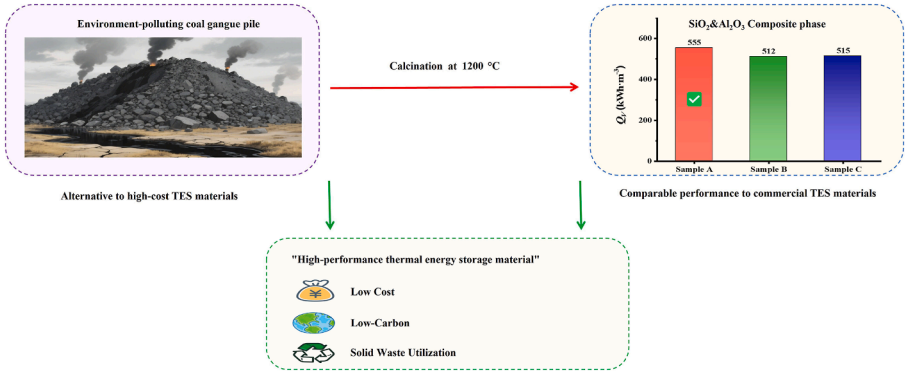

ARTICLE INFO

Keywords:
Sensible heat storage materials
Coal gangue
Volumetric heat storage density
Solid waste beneficiation

ABSTRACT

Thermal energy storage (TES) is a key enabler for the large-scale utilization of intermittent renewable energy sources like solar and wind power, and it also offers an efficient pathway for industrial electrification and decarbonization. However, the widespread adoption of TES is hindered by the high cost of conventional TES materials, such as alumina, magnesium oxide, and other ceramics. This study investigates the feasibility of converting coal gangue, an abundant industrial waste with considerable environmental impact, into a low-cost, mechanically stable, and thermally efficient material for medium-to high-temperature sensible heat storage applications. Three representative coal gangue samples from the Ordos region in Inner Mongolia, China, were calcined at temperatures ranging from 1000 to 1300 °C to optimize their phase compositions, mechanical strengths, and thermophysical properties. Among the samples, Sample A from Jungar exhibited the best overall performance, achieving a volumetric heat storage density of approximately 555 kWh m^{-3} at 1200 °C, which is comparable to typical sensible heat storage materials, while maintaining good mechanical integrity and satisfactory cyclic stability. With near-zero raw-material cost, a simple single-step preparation process, and potential policy incentives for solid-waste utilization, the coal-gangue-based composites developed here offer clear

* Corresponding author. Beijing Key Laboratory of Green Chemical Reaction Engineering and Technology, Department of Chemical Engineering, Tsinghua University, Beijing, 100084, China.
** Corresponding author.
E-mail addresses: cxzhang@tsinghua.edu.cn (C. Zhang), drbai@syuct.edu.cn (D. Bai).

https://doi.org/10.1016/j.partic.2026.05.015
Received 4 April 2026; Received in revised form 14 May 2026; Accepted 21 May 2026
Available online 29 May 2026

economic and environmental advantages and introduce a promising, low-cost material system for sustainable TES applications at medium-to high-temperature levels.

1. Introduction

The rapid expansion of wind and solar power has become a defining trend in today's energy landscape. However, the inherent intermittency and variability of renewable energy can create temporal mismatches between power supply and demand, limiting stable grid integration and efficient utilization (Shair et al., 2021). In this context, high-temperature thermal energy storage (HT-TES) technologies provide a promising solution by storing surplus energy as heat in solid media or molten salts and releasing it on demand for industrial heating and steam generation, thereby improving overall energy utilization and economic performance (Ali et al., 2024; Ge et al., 2014; Liu, Li, et al., 2025).

At present, the large-scale application of solid-particle-based HT-TES systems is partly constrained by the relatively high cost of storage materials (Alva et al., 2017; Calderón et al., 2018; Wang et al., 2025). Consequently, increasing attention has been directed toward the development of low-cost materials with high thermal stability. Among the feasible approaches, recycling industrial solid wastes as thermal storage media has emerged as a promising strategy for reducing material costs while promoting resource utilization (Kocak et al., 2021a, 2021b; Xiong et al., 2025; Kocak & Paksoy, 2020).

Coal gangue, a major by-product of coal mining, possesses physicochemical characteristics suitable for sensible heat storage applications (Fu & Wang, 2024). Large quantities of coal gangue are generated annually in China, adding to extensive stockpiles that occupy land resources and pose increasing risks of dust pollution and ecological damage. For example, Ordos City in Inner Mongolia, a region rich in coal reserves, generates coal gangue that accounts for approximately 60% of the local industrial solid waste, as illustrated in Fig. 1(a) and (b) (Rijimoleng & Gang, 2018). From the perspectives of waste valorization and resource recycling, utilizing coal gangue to fabricate sensible heat storage materials offers a promising pathway for developing low-cost solid particles for HT-TES systems, while simultaneously reducing accumulated waste and mitigating the environmental impacts associated with long-term disposal (Gao et al., 2024; Zhang et al., 2025).

Based on the aforementioned background and needs, this study investigates the feasibility of converting coal gangue into medium-to high-temperature sensible heat storage materials. Through a one-step high-temperature calcination process, coal gangue was successfully transformed into ceramic-based composite heat storage media, which were systematically characterized. The results demonstrate that the composite heat storage media exhibit promising thermal storage performance, stable thermophysical properties, and satisfactory cyclic durability, highlighting their potential for medium-to high-temperature TES applications. This work provides a practical pathway for developing low-cost HT-TES materials while promoting the resource utilization of coal gangue solid waste.

2. Materials and methods

2.1. Materials

Three coal gangue raw materials were collected from different regions of Ordos City — Jungar (raw material A), Yijinholuo (raw material B), and Wushen (raw material C) — using bulk-solid sampling procedures. The samples were analyzed using X-ray fluorescence (XRF), and the results are shown in Table 1. The primary components of raw materials A, B, and C are SiO_2 and Al_2O_3, with their combined mass ratio exceeding 80%. The remaining content consisted of small amounts of SO_3, Fe_2O_3, TiO_2, and K_2O.

The molar ratios of Al_2O_3 to SiO_2 (denoted as the Al_2O_3/SiO_2 ratio) of the three raw materials were calculated based on the mass ratios of Al_2O_3 and SiO_2. As shown in Fig. 2(a), the Al_2O_3/SiO_2 ratio ranges from 0.28 to 0.56 for these materials. Fig. 2(b–d) show the X-ray diffraction patterns of the three raw materials. The main diffraction peaks of all the three materials correspond to kaolinite (PDF#03-0052) and quartz (PDF#46-1045). Compared with raw material A, raw materials B and C exhibit stronger quartz diffraction peaks, indicating a higher quartz content, consistent with the XRF results. In addition, small amounts of metal oxides are present in all three samples.

2.2. Methods

To prepare the experimental samples, the raw materials were first crushed and sieved to obtain particles in the size range of 10–20 mesh (830–1700 μm), which provides a balance among heat transfer

Table 1
Main components and contents (mass%) of the coal gangue raw materials.

Samples	Components					
	SiO_2	Al_2O_3	SO_3	Fe_2O_3	TiO_2	K_2O
Raw material A	44.64	42.16	5.42	3.28	2.06	0.29
Raw material B	55.93	35.11	4.65	4.61	1.33	1.61
Raw material C	56.35	26.43	4.12	5.02	1.20	3.27

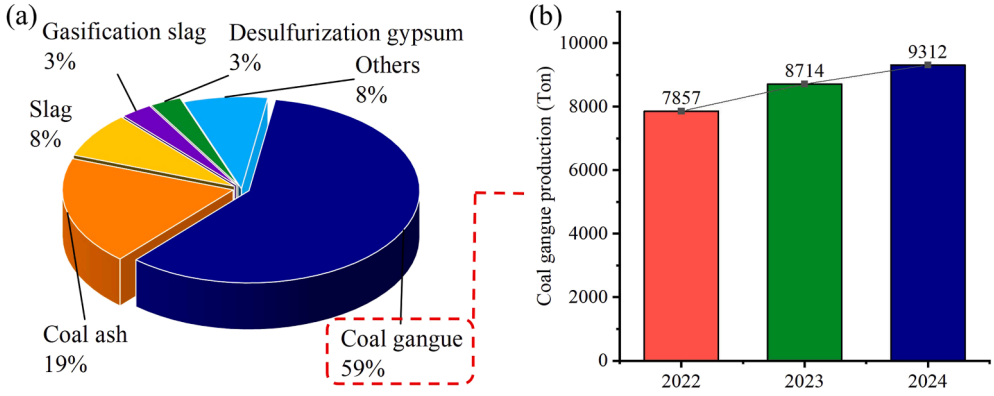

Fig. 1. (a) Proportion of industrial solid waste in 2024 and (b) production of coal gangue in recent years (data source: Ordos Municipal Bureau of Ecology and Environment).

performance, wear resistance, and anti-caking behavior, particularly for packed-bed applications (Zeng et al., 2025). A measured quantity of particles was then placed in an alumina crucible and heated in air at 10 K/min to 1200 °C, maintained for 120 min, and naturally cooled to room temperature inside the furnace at an average cooling rate of approximately 5 K/min.

The optimal preparation conditions were determined based on a performance index defined as the product of the specific heat capacity and bulk density of the sample. A stepwise optimization procedure was adopted. First, the index values of samples prepared at different calcination temperatures were compared to identify the optimal temperature. Next, samples prepared at the selected temperature using different heating rates were evaluated to determine the optimal heating rate. Finally, samples prepared under the optimized temperature and heating rate conditions but with different holding times were compared to identify the most suitable holding time. Detailed results are provided in Supplementary Table S1. The samples prepared under the optimized thermal treatment conditions were designated as Sample A, Sample B, and Sample C.

The phase compositions of the samples were characterized using a Bruker D8 Advance X-ray diffraction (XRD) instrument at a scanning speed of 2°/min. Based on the XRD patterns, the phases were identified by matching characteristic peaks to the standard powder diffraction file (PDF) cards, and their relative abundances were assessed by comparing peak intensities and peak shapes (e.g., full width at half maximum (FWHM)) of the strongest peaks. The microstructure was observed using a Zeiss Sigma 300 scanning electron microscope (SEM). The true densities were measured using an AccuPyc II 1345 gas pycnometer. The bulk density of naturally packed particles was determined using the standard container method. The hardness was tested using a hardness tester (ZongDe Machine HVZHT-50). The specific surface area and pore structure parameters were calculated from N_2 adsorption–desorption isotherms measured using a Micromeritics ASAP 2460, with the specific surface area determined using the Brunauer–Emmett–Teller (BET) method. The specific heat capacity was measured using a TA DSC25 differential scanning calorimeter (DSC). The thermal diffusivity was measured using a Netzsch LFA427 laser-flash apparatus.

3. Results and discussion

3.1. Phase composition and microstructure analysis

Fig. 3 presents the mass change and phase evolution of three raw materials at various activation temperatures. The results indicate that after calcination at 1000 °C, the main phases in the calcined products are primarily Al–Si spinel and mullite, along with a minor amount of quartz. This suggests that the Al and Si elements in the raw materials react to form Al–Si spinel and mullite, while some quartz remains due to its excess in the raw materials. At 1100 °C, the mass loss of all three raw materials stabilizes (Fig. 3(a)), and the diffraction peaks of mullite significantly intensify (Fig. 3(b–d)), whereas the diffraction peaks of Al–Si spinel decrease, indicating that Al–Si spinel continues to react and gradually transforms into mullite. At 1200 °C, the diffraction peaks of mullite continue to increase, whereas those of Al–Si spinel vanish, indicating the complete transformation of Al–Si spinel into mullite. Previous studies have reported that kaolinite ($Al_2Si_2O_5(OH)_4$) dehydroxylates at approximately 600 °C to form metakaolin, which then transforms into Al–Si spinel between 900 and 1000 °C. When the temperature reaches 1000–1200 °C, Al–Si spinel undergoes a complete transformation to mullite, as described by reactions (1–3) (Hu et al., 2023; Xu et al., 2018):

$$2Al_2Si_2O_5(OH)_4(\text{Kaolinite}) \text{—} 2Al_2Si_2O_7(\text{Metakaolin}) + 4H_2O\ (600\ ^\circ\text{C}) \quad (1)$$

$$2Al_2SiO_7 \text{—} Si_3Al_4O_{12}(\text{Spinel}) + SiO_2\ (900\text{-}1000\ ^\circ\text{C}) \quad (2)$$

$$3Al_2Si_2O_7 \text{—} Si_2Al_6O_{13}(\text{Mullite}) + 4SiO_2\ (1000\text{-}1200\ ^\circ\text{C}) \quad (3)$$

At 1300 °C, the diffraction peaks of all samples show minimal changes, indicating that the reactions are almost complete at 1200 °C. A comparison of the XRD patterns of the different samples reveals a decrease in the intensity of the mullite diffraction peaks in the order of Samples A, B, and C. In contrast, the relative intensity of the quartz diffraction peaks increases correspondingly. This suggests that as the Al_2O_3/SiO_2 ratio in the raw materials decreases (Table 1), the relative content of mullite in the final composite decreases, whereas the relative content of quartz increases.

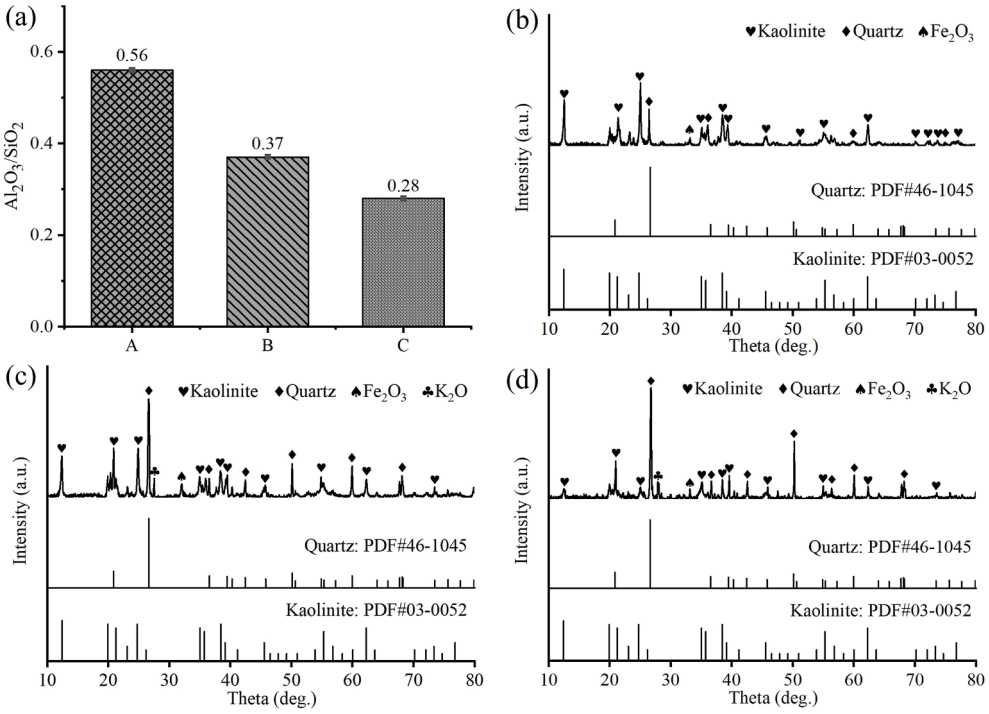

Fig. 2. (a) Al_2O_3/SiO_2 molar ratios of raw materials and XRD diffraction patterns of (b) raw material A, (c) raw material B, and (d) raw material C.

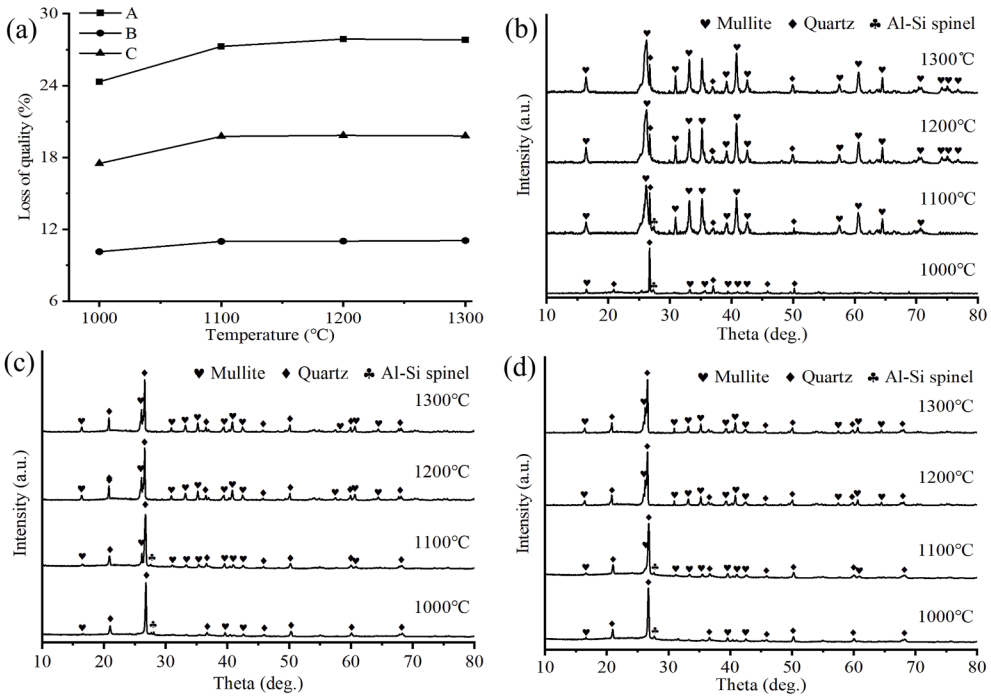

Fig. 3. (a) Mass loss of raw materials and XRD diffraction patterns of (b) raw material A, (c) raw material B, and (d) raw material C at different activation temperatures.

Fig. 4 presents the microstructures of the samples, along with the corresponding EDS analysis results based on phase-composition analysis. All three samples exhibit continuous and dense microstructures with no visible pores, indicating sufficient sintering. EDS analysis reveals a high spatial co-localization of Al and Si, confirming the formation of a stable mullite structure in the matrix. Distinct spherical glassy phases are observed on the surfaces of Samples B and C (regions 1, 2, and 3 in this figure), whereas no such features are present in Sample A. This microstructural difference is primarily attributed to variations in the original chemical composition: Samples B and C have a lower Al_2O_3/SiO_2 ratio, particularly after accounting for the volatilization of the SO_3 component at high temperatures. This leads to a relatively higher effective content of K_2O and Fe_2O_3. At elevated temperatures, the excess SiO_2 reacts with K_2O to form a potassium silicate liquid phase. Constrained by reaction kinetics, this liquid phase solidifies into an amorphous glass phase upon cooling (Koroleva et al., 2023), with Fe_2O_3 acting as a flux that readily incorporates into this glassy matrix (Wang, Tang, et al., 2022). Although the glass phase contributes to material densification, it significantly impacts thermal conductivity by acting as phonon scattering centers. Furthermore, an increased glass phase content exacerbates the thermal expansion mismatch at the interfaces with quartz and mullite, thereby raising the probability of microcrack formation during thermal cycling. This consequently limits the material's thermal conductivity and long-term cyclic stability (Wang, Tang, et al., 2022).

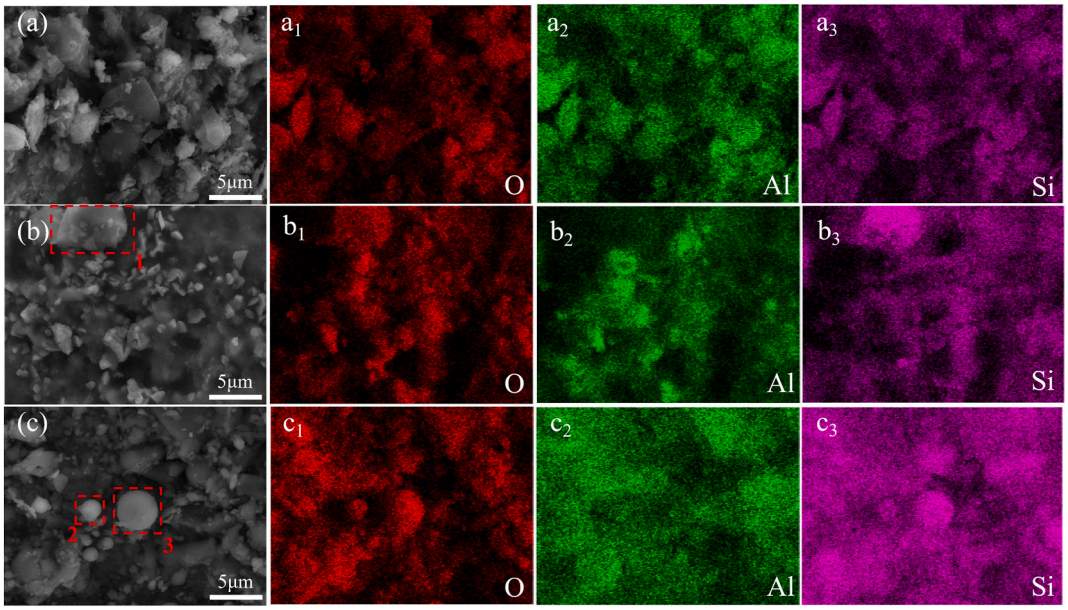

Fig. 4. Microstructure and EDS of (a) Sample A, (b) Sample B, and (c) Sample C, and the corresponding element distributions of the samples.

Based on the combined phase composition and microstructure analysis, Sample A exhibits more favorable material characteristics. Its higher relative mullite content and significantly lower glassy phase content provide a critical material foundation for achieving superior sensible heat storage performance and long-term cycling stability.

3.2. Physical adsorption and mechanical properties

Fig. 5 presents the nitrogen adsorption–desorption isotherms (Fig. 5 (a)) and corresponding pore-size distribution curves for the three samples. Despite the differences in chemical composition, the isotherms for Samples A, B, and C can all be classified as Type II according to the IUPAC guidelines (Rahman et al., 2019). Prominent H4-type hysteresis loops with relatively flat desorption branches are observed in the medium-to-high relative-pressure region, indicating predominantly slit-shaped pores and the coexistence of micropores and mesopores (Wang & Guo, 2020). The pore size distribution curves (Fig. 5(b)) further support this interpretation: the pore sizes for all three samples are mainly concentrated in the micropore and small mesopore ranges, with relatively narrow distributions and virtually no macropores. From Sample A to Sample C, the peak intensity of the pore size distribution increases gradually. It shifts slightly toward smaller pore diameters, suggesting an increase in the number and fraction of small pores and a more developed pore structure. This trend is consistent with the large hysteresis loop area observed in the isotherms.

As listed in Table 2, from Samples A to C, the specific surface area, porosity, and pore volume increase gradually, indicating that the number of pores and total pore volume fraction are progressively rising, and the pore structure evolves from relatively sparse to a more developed porous framework. Overall, the porosity of all three samples remains low, indicating a dense framework structure with a small number of micro- and mesopores. For sensible heat storage materials, an appropriate pore structure benefits heat transfer. However, excessively high porosity can reduce the bulk density and thermal conductivity, thereby weakening its heat storage capacity and charging-discharging efficiency (Chen et al., 2024; Dionne et al., 2024). Therefore, a balance must be maintained between the pore structure parameters and sensible heat storage performance.

To further evaluate the suitability of the three samples for sensible heat storage from the perspective of macroscopic physical properties, their true density, bulk density, and high-temperature hardness were measured. Fig. 6(a) shows the true and bulk densities of three samples. Sample A exhibits the highest true density, whereas Samples B and C show slightly lower values. This trend correlates well with differences in the mullite and quartz contents among the samples: a higher proportion of mullite leads to an increase in true density (Romero et al., 2021). The bulk densities of all three samples are significantly lower than their true densities, reaching only approximately 60% of the latter, indicating a high-volume fraction of interparticle voids formed during particle packing. These interparticle voids contribute to the overall volume but hardly to the mass, thereby reducing the macroscopic bulk density and directly influencing the volumetric heat storage density of the materials (Lai et al., 2022).

Table 2
Specific surface area, porosity, and pore volume of the samples.

Samples	Specific surface area (m^2 g^{-1})	Porosity (%)	Pore volume (cm^3 g^{-1})
Sample A	15.07	3.13	0.0125
Sample B	15.32	3.13	0.0131
Sample C	15.96	3.21	0.0137

Based on the density results, the high-temperature hardness was further examined to assess the mechanical stability. Fig. 6(b) shows the hardness–temperature curves for the three samples. At room temperature, Sample A exhibits the highest hardness owing to its higher mullite content. In contrast, Samples B and C display lower and similar hardness values, consistent with their mineralogical compositions. As the temperature increases, the hardness of all three samples decreases monotonically. In the range of 25–1200 °C, the hardness of Sample A decreases by approximately 31%, whereas that of Samples B and C, which contain higher quartz contents, decreases by approximately 57%. The hardness decrease under high-temperature conditions primarily stems from intrinsic thermal softening mechanisms, such as weakened atomic bonding and thermal activation of dislocation motion (Kamimura et al., 2013). The differences between the samples stem from the starkly contrasting high-temperature behaviors of mullite and quartz: mullite maintains a relatively stable framework structure at elevated temperatures, with its hardness reduction primarily attributed to lattice softening. In contrast, quartz undergoes a phase transition near 570 °C, accompanied by significant volume expansion (Dal et al., 2023), generating immense thermal stresses within the material that disrupt the framework integrity and cause a sharp decline in the high-temperature hardness.

The above analysis systematically characterizes the differences in the macroscopic physical properties of the samples, including porosity, bulk density, and high-temperature hardness. These parameters jointly determine the available sensible heat storage volume and structural stability of the materials in practical applications and are thus key indicators for evaluating their sensible heat storage performance.

3.3. Specific heat capacity and heat storage density

The specific heat capacity (C_P) is a key parameter for characterizing sensible heat storage performance, as it directly determines the amount of heat that can be stored per unit mass of a material under a given

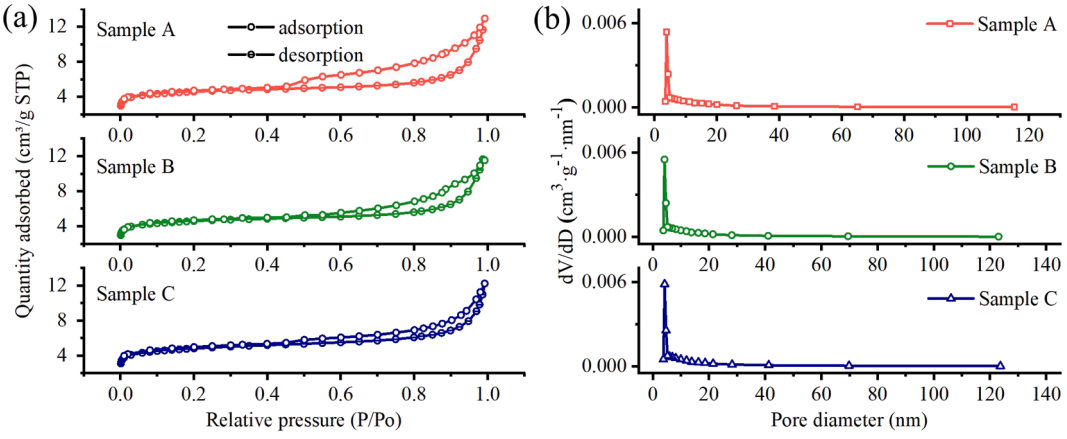

Fig. 5. (a) Nitrogen adsorption–desorption isotherms and (b) pore size distribution curves of the samples.

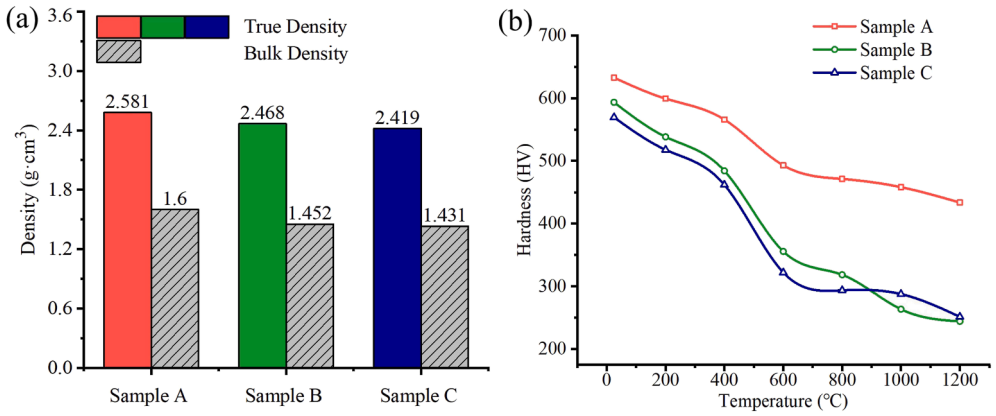

Fig. 6. (a) True density and bulk density of the samples, and (b) hardness of the samples as a function of temperature.

temperature difference. Fig. 7(a) shows the variation in C_P with temperature for three samples. The values of C_P increase with temperature for all three samples, reflecting typical thermodynamic behavior: lattice vibrations intensify at high temperatures, activating more vibrational modes and thereby enhancing the material's heat absorption capacity (Wen et al., 2015). In the temperature range of approximately 600–800 °C, the slope of the C_P-temperature curve increases noticeably, indicating accelerated growth. This interval corresponds to the α→β phase transition of quartz near 573 °C (Dal et al., 2023). This transition involves lattice rearrangement and volume change, and the associated enthalpy change manifests as a sharp increase in the effective C_P (Breuer & Schilling, 2021). Samples B and C, which contain higher quartz contents, exhibit a larger increase in C_P in this range than Sample A, consistent with their mineralogical compositions.

Based on the above C_P results, the three samples exhibit similar C_P values in the high-temperature region, with approximately 1.06, 1.08, and 1.10 J g^{-1} K^{-1} at 1200 °C. This indicates that, when evaluated on a mass basis, the differences in sensible heat storage capacity among the samples are relatively small. However, in practical thermal energy storage systems, the volume available for storage units is strictly constrained by system layout and structural conditions. Therefore, maximizing the heat storage capacity within a limited space is crucial for improving overall system performance. To reflect the heat-storage behavior of materials under such conditions, it is necessary to characterize their performance from a volumetric perspective by introducing the volumetric heat storage density (Q_V), defined as

$$Q_V = \int_{T1}^{T2} \rho_b \, C_p \, dT \tag{4}$$

Where ρ_b is the bulk density (which changes little with temperature so the value measured at room temperature was adopted here), and T_1 and T_2 are the initial and final temperatures, respectively. In this study, T_1 is fixed at 25 °C, and T_2 represents the maximum operating temperature tested.

Fig. 7(b) shows the variation in Q_V with temperature for the three samples. For all samples, Q_V increases monotonically over the investigated temperature range, with curves exhibiting a slightly convex upward trend; the increase is relatively small at lower temperatures but gradually accelerates as the temperature rises, reflecting the cumulative effect of temperature-dependent $Cp(T)$ in Eq. (4). In contrast to the Cp curves in Fig. 7(a), which exhibit a pronounced change in slope at approximately 600–800 °C due to the α→β phase transition of quartz, the Q_V-temperature curves show no obvious abrupt anomalies in this region. The integration over temperature smears out the phase-transition effect, manifesting only as a moderate enhancement of the Q_V's high-temperature growth rate.

Over the entire temperature range, Sample A exhibits a slightly higher Q_V than Samples B and C. In contrast, the curves of Samples B and C almost overlap, indicating that the Q_V of the three materials is close, with Sample A having a modest but persistent advantage. The inset in Fig. 7(b) shows the Q_V at 1200 °C. At this temperature, the Q_V values for Samples A, B, and C are approximately 555, 512, and 515 kWh m^{-3}, respectively. The small but consistent superiority of Sample A can be attributed to its higher mullite content and more compact skeletal structure, which result in a slightly higher bulk density and thus a larger amount of heat-storage mass per unit volume. Samples B and C, with higher quartz contents and somewhat more developed pore structures, show correspondingly lower bulk densities and Q_V values. These results

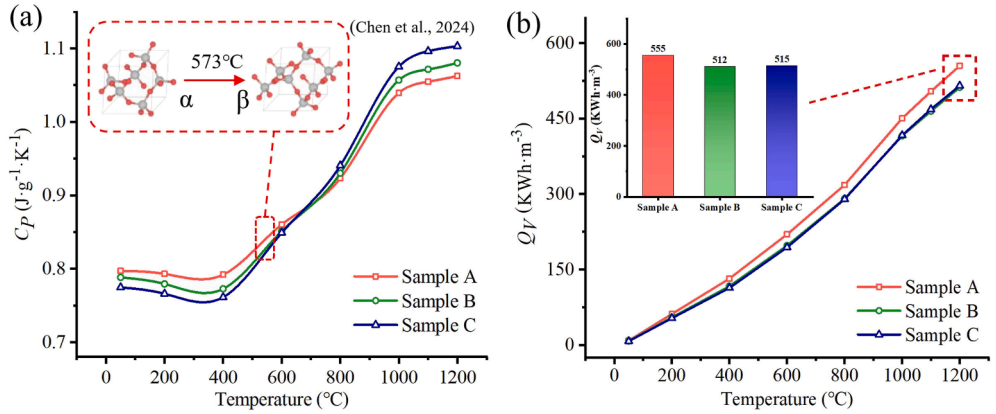

Fig. 7. (a) C_P and (b) Q_V of the samples as a function of temperature. The x-axis in (b) corresponds to T_2 in Eq. (4). (insets: crystal phase transition in (a) and Q_V at 1200 °C in (b)).

highlight that, for volume-constrained sensible heat storage systems, optimizing bulk density through phase composition and microstructural design can be as important as tailoring *Cp*. Compared with commercial sensible heat storage materials reported in the literature (Khare et al., 2013), all three samples exhibit relatively high Q_V in the medium-to-high temperature range, demonstrating good application potential, with Sample A being relatively superior.

3.4. Thermal conductivity

Based on the foregoing analysis of Q_V, a more objective and comprehensive evaluation of the overall sensible heat storage performance of the three samples requires that their heat-transfer characteristics also be taken into account. Accordingly, the present section focuses on the thermal conductivity of the materials and their temperature dependence.

The thermal diffusivities (D) of the three samples were first measured as a function of temperature, as shown in Fig. 8(a). It can be seen that D of all three samples increases monotonically with temperature and reaches a maximum at around 1200 °C. Over the entire temperature range, Sample A maintains the highest D, followed by Sample B and C. This trend is highly consistent with the previously observed trends in bulk density and pore structure characteristics: Sample A has a higher bulk density and lower total porosity, along with a higher mullite content and a more continuous, compact skeletal framework. As a result, interfacial phonon scattering and pore-related thermal resistance are relatively weak, which facilitate effective phonon transport through the solid framework. By contrast, Samples B and C contain a higher proportion of quartz and slightly more developed pores and grain boundaries, which enhance phonon scattering and interfacial thermal resistance, resulting in lower D.

On this basis, the thermal conductivity (κ) of the materials was calculated from the measured D using the following relation (Agne et al., 2019):

$$\kappa = C_p \, D \, \rho_b \tag{5}$$

The variations of κ with temperature for the three samples are presented in Fig. 8(b). It is evident that the κ values of all three samples increase with increasing temperature and reach a maximum at approximately 1200 °C. Since the differences in C_P among the three samples are relatively small, the variations in κ are mainly governed by the combined effects of ρ_b and D. Owing to its higher mullite content and denser skeletal structure, Sample A exhibits larger ρ_b and D values and therefore attains the highest κ. Samples B and C, with higher quartz contents and more developed interfaces and pores that induce stronger phonon scattering, show slightly lower ρ_b and D, and consequently somewhat lower κ than Sample A.

From the perspective of sensible heat storage materials, thermal conductivity (κ) is an important property in addition to heat storage capacity, as it affects heat charging/discharging rates and temperature uniformity within particles, particularly in packed-bed systems. In fluidized beds, although overall heat transfer is dominated primarily by convective effects, it still plays an important role in determining heat transfer performance at the particle scale (Díaz-Heras et al., 2020). In combination with the Q_V results, these findings indicate that Sample A, which exhibits both relatively high Q_V and superior κ, is particularly favorable for practical applications requiring fast, efficient heat storage. Samples B and C, although slightly inferior to Sample A in terms of κ, remain within the same order of magnitude and thus retain application potential in medium-to high-temperature sensible heat storage systems.

3.5. Cyclic stability under heating and cooling conditions

To evaluate the service reliability and lifetime of the sensible heat storage materials under frequent high-temperature (heat charging) and low-temperature (heat discharging) cyclic conditions, the three samples were subjected to 50 heating–cooling cycles between 25 and 1200 °C. This cycle number was selected as a preliminary screening protocol to identify relative stability trends among the three samples, with comprehensive long-term cycling studies (over 500 cycles) planned for the optimized composition in future work. Before and after thermal cycling, the Q_V and hardness of the materials at 1200 °C were measured, and the corresponding retention (R) was calculated as P_n/P_0, where P_n and P_0 represent the performance after n cycles and the initial performance, respectively.

Fig. 9(a) shows the Q_V values and R (inset of Fig. 9(a)) for the three samples at 1200 °C before and after cycling. After thermal cycling, the Q_V at 1200 °C decreases only slightly, with an R value of approximately 94%, indicating that the Q_V does not degrade significantly after thermal cycles. In addition, no visible breakage or cracking was observed on the sample surfaces after thermal cycling, despite exposure to temperatures as high as 1200 °C. Further insights into mechanical and structural stability can be gained from the high-temperature hardness, which is a sensitive indicator of internal damage accumulation. As shown in Fig. 9 (b), the high-temperature (1200 °C) hardness of all samples exhibits a decreasing trend as the number of thermal cycles increases. Among them, Sample A shows the greatest decrease, yet its high-temperature hardness remains the highest, with an R as high as 85%. Thus, this indicates that its high-temperature mechanical properties degrade slowly and its internal structure is relatively stable, which is attributed to the high content of mullite in the sample.

Overall, after 50 thermal cycles between 25 and 1200 °C, all three samples show little degradation in either Q_V or high-temperature hardness, indicating good preliminary cyclic stability. This structural integrity also helps mitigate the risk of trace element leachability or dust release during thermal cycling (Deb et al., 2025). Among the three samples, Sample A possesses both a high Q_V and an excellent high-temperature hardness, demonstrating superior overall cyclic performance for medium-to high-temperature sensible heat storage applications.

4. Assessment of economic potential

The utilization of coal gangue as a sensible heat storage material offers significant advantages in terms of resource availability, economic viability, and environmental sustainability. In this study, the production cost was evaluated using a unit-cost accounting approach, in which the total cost was estimated by summing expenses associated with raw materials, energy consumption, transportation, pretreatment, and auxiliary operations under representative industrial conditions.

Recent statistics indicate that the cumulative stockpile of coal gangue in China exceeds 7 billion tons, with an annual new generation of approximately 7×10^8 to 8.5×10^8 tons (Du et al., 2025; Gong et al., 2025). Major coal-producing regions such as Ordos generate tens of millions of tons annually, providing abundant and accessible waste resources for industrial reuse. In many mining areas, coal gangue is available at zero (or even negative) procurement cost because coal enterprises must otherwise bear disposal and environmental management expenses (Liu, Li, et al., 2025).

Given this near-zero raw material cost, the overall production cost is essentially dominated by calcination energy consumption and auxiliary operational expenses. The calcination energy cost was estimated using the average industrial electricity price in Ordos, Inner Mongolia (≈0.07 USD kWh^{-1}) together with the theoretical energy demand of the thermal treatment process. The process involved heating the raw material from room temperature (25 °C) to 1200 °C at 10 K min^{-1}, followed by a 120 min holding stage. Assuming an average specific heat capacity of 0.9 kJ kg^{-1} K^{-1}, the theoretical electricity consumption was estimated to be approximately 441 kWh per ton of raw material, corresponding to an energy cost of about 31 USD t^{-1}.

Auxiliary costs, including raw material collection, transportation, crushing, screening, and impurity removal, were estimated based on

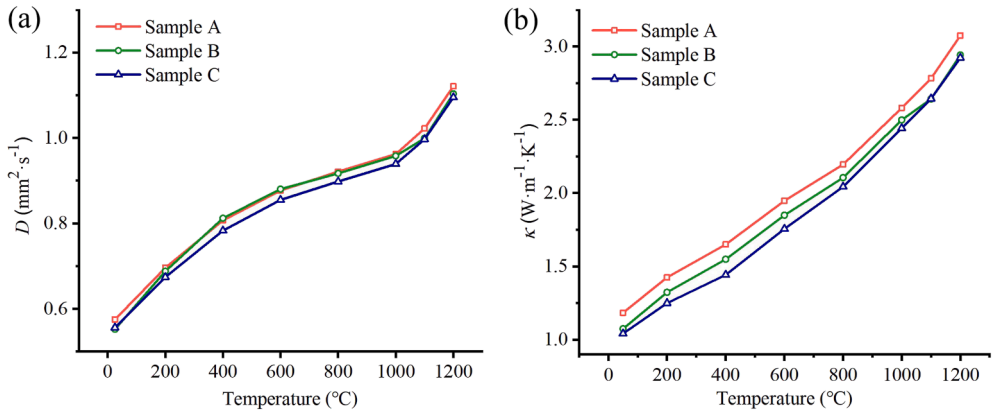

Fig. 8. (a) D and (b) κ of the samples as a function of temperature.

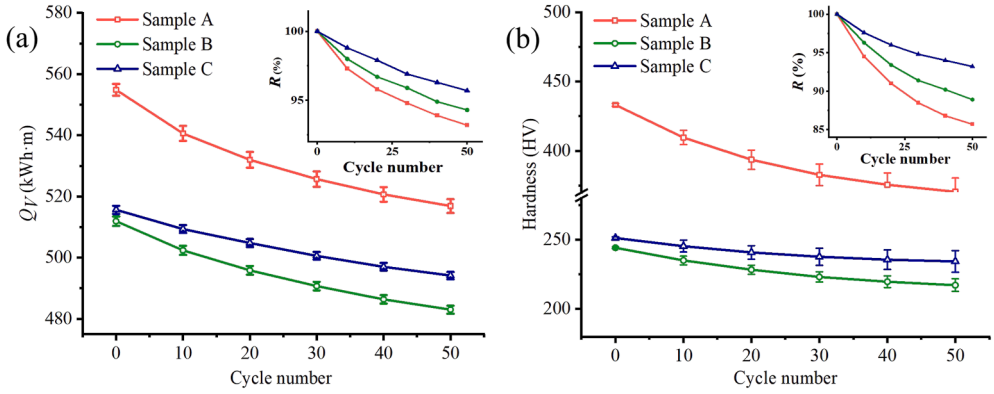

Fig. 9. Cycling performance of (a) Q_V and (b) hardness at 1200 °C. (inset: corresponding performance retention).

typical industrial practices and regional operating conditions. Collection and stockpiling costs were estimated at 1–3 USD t^{-1}, transportation costs at 4–6 USD t^{-1} for haulage distances of 40–60 km, and pretreatment costs at 2–3 USD t^{-1}. Accordingly, the total auxiliary operational cost was estimated to range from 7 to 12 USD t^{-1}, with a representative value of approximately 10 USD t^{-1} adopted for the overall assessment.

Table 3 lists the estimated cost of coal-gangue-derived composite storage materials and comparison with white corundum and nitrate molten salts.

By combining the estimated energy and auxiliary operational costs, the total production cost of the coal gangue-based composite material was calculated to be approximately 41 USD t^{-1}. Although these values are approximate estimates derived from representative industrial parameters and regional market conditions rather than direct plant measurements, they provide a transparent and reproducible basis for economic evaluation. Importantly, the estimated cost is lower than that of conventional sensible heat storage materials such as white corundum and molten salts (Caraballo et al., 2021; Zhao et al., 2022), highlighting the strong economic potential of the developed composite material.

Table 3
Estimated cost of coal-gangue-derived composite storage materials and comparison with white corundum (Al_2O_3) and nitrate molten salts.

Material	Origin	Price range (USD/ton)	Operating temp. (°C)	Unit price (USD/kWh)
Coal gangue	Mining waste	30–40	25–1200	0.12 (25–1200 °C)
White corundum	Synthetic	1200–1800	25–1200	3.4 (25–1200 °C)
Nitrate molten salt	Synthetic	770–1200	25–560	3.3 (25–560 °C)

Notes: Unit price (USD/kWh) was calculated by converting the volumetric heat-storage capacity (kWh/m^3) to a gravimetric basis (kWh/ton) using the bulk density, and then dividing the material price (USD/ton) by the obtained kWh/ton.

In addition, employing coal gangue as a raw material for TES can help reduce the environmental burden associated with its long-term stockpiling. Previous studies have shown that the comprehensive utilization of 1 t of coal gangue can reduce long-term land occupation by approximately 1.2–1.5 m^2 and mitigate dust emissions and leachate pollution arising from large-scale dumping (Gong et al., 2020; Li & Wang, 2019). Under the current solid-waste resource utilization policies in regions such as Ordos, coal gangue utilization projects may also be eligible for tax reductions and other policy incentives, which further enhance the economic feasibility of coal gangue-based composites for medium-to high-temperature sensible heat storage applications.

5. Conclusion

In this study, coal gangue from different regions of Ordos was used as the raw material and successfully converted, via a single-step high-temperature calcination at 1200 °C, into mullite–quartz-based composite materials for medium-to high-temperature sensible heat storage. All three samples exhibit stable phase compositions, good overall mechanical integrity and favorable thermophysical properties in the temperature range of 25–1200 °C, among which Sample A shows the most balanced property profile, combining a relatively high volumetric sensible heat storage density (about 555 kWh m^{-3} at 1200 °C), higher thermal conductivity, good high-temperature hardness and satisfactory short-term cyclic stability. Taking into account the abundant resource

base and very low raw-material cost of coal gangue, together with the comparatively low energy and processing costs of the single-calcination route, coal gangue-based composites can be regarded as a technically feasible and economically attractive candidate system for medium-to high-temperature sensible heat storage when compared with commercial materials such as white corundum and typical molten salts. This work provides a viable pathway for the high-value utilization of coal gangue, presenting a new low-cost, high-performance material for sensible heat storage and medium-to high-temperature industrial waste-heat recovery.

CRediT authorship contribution statement

Lei Zhang: Writing – review & editing, Writing – original draft, Data curation, Supervision, Conceptualization. **Chenxi Zhang:** Conceptualization, Supervision. **Zezhong Wang:** Writing – original draft, Data curation. **Xingbo Zhao:** Writing – original draft, Data curation. **Jing Shen:** Resources. **Dingrong Bai:** Writing – review & editing, Supervision, Conceptualization.

Declaration of competing interest

The authors declare that they have no known competing financial interests or personal relationships that could have appeared to influence the work reported in this paper.

Acknowledgments

We acknowledge the financial support provided by the Inner Mongolia Government under the project “Research and Development of Key Technologies for Novel High-Temperature Industrial Thermal Energy Storage Systems” (Project number: Ordoslab-2023002).

Appendix A. Supplementary data

Supplementary data to this article can be found online at https://doi.org/10.1016/j.partic.2026.05.015.

Nomenclature

BET	Brunner–Emmet–Teller
C_P	Specific heat capacity
D	Thermal diffusivity
EDS	Energy Dispersive Spectroscopy
FWHM	Full Width at Half Maximum
HT-TES	High-Temperature thermal energy storage
IUPAC	International Union of Pure and Applied Chemistry
PDF	Powder Diffraction File
Q_V	Volumetric thermal storage
TES	Thermal energy storage
XRD	X-ray diffraction
XRF	X-ray fluorescence
κ	Thermal conductivity

References

Agne, M. T., Voorhees, P. W., & Snyder, G. J. (2019). Phase transformation contributions to heat capacity and impact on thermal diffusivity, thermal conductivity, and thermoelectric performance. *Advanced Materials, 31*(35), Article 1902980.

Ali, H. M., Rehman, T.-u., Arıcı, M., et al. (2024). Advances in thermal energy storage: Fundamentals and applications. *Progress in Energy and Combustion Science, 100*, Article 101109.

Alva, G., Liu, L., Huang, X., et al. (2017). Thermal energy storage materials and systems for solar energy applications. *Renewable and Sustainable Energy Reviews, 68*, 693–706.

Breuer, S., & Schilling, F. R. (2021). Anisotropic thermal transport properties of quartz: From −120 °C through the α–β phase transition. *European Journal of Mineralogy, 33*, 23–38.

Calderón, A., Palacios, A., Barreneche, C., et al. (2018). High temperature systems using solid particles as TES and HTF material: A review. *Applied Energy, 213*, 100–111.

Caraballo, A., Galán-Casado, S., Caballero, Á., et al. (2021). Molten salts for sensible thermal energy storage: A review and an energy performance analysis. *Energies, 14*, 1197.

Chen, Z., Yu, C., Ge, Y., et al. (2024). Interface phonon scattering suppression boosts heat conduction in thermal interface materials. *Chemical Engineering Journal, 500*, Article 156924.

Dal Bo, M., Gilabert, F. A., Ortega Boschi, A., et al. (2023). Influence of beta-to-alpha quartz transition on residual stresses of a feldspar glass matrix composite: A relationship with catastrophic fracture due to thermal shock. *Journal of the European Ceramic Society, 43*, 4562–4572.

Deb, R., Iqbal, M. I., & Farnam, Y. (2025). Evaluating long-term thermal and chemical stability and leaching potential of low-temperature phase change materials in concrete slabs exposed to outdoor environmental conditions. *Materials and Structures, 23*, 58.

Díaz-Heras, M., Belmonte, J. F., & Almendros-Ibáez, J. A. (2020). Effective thermal conductivities in packed beds: Review of correlations and its influence on system performance. *Applied Thermal Engineering, 171*, Article 115048.

Dionne, C. J., Thakur, S., Scholz, N., et al. (2024). Enhancing the thermal conductivity of semiconductor thin films via phonon funneling. *npj Computational Materials, 10*, 177.

Du, P., Ren, Y., Liu, Z., et al. (2025). From waste to resources: Coal gangue utilization-A comprehensive analysis. *Process Safety and Environmental Protection, 201*, Article 107558.

Fu, H., & Wang, W. (2024). Characterization of coal gangue and fabrication of porous ceramic materials. *Ceramics-Silikáty, 68*(1), 80–87.

Gao, L., Liu, Y., Xu, K., et al. (2024). A short review of the sustainable utilization of coal gangue in environmental applications. *RSC Advances, 14*, 39285–39296.

Ge, Z., Li, Y., Li, D., et al. (2014). Thermal energy storage: Challenges and the role of particle technology. *Particuology, 15*, 2–8.

Gong, Y., Hu, Z., & McSweeney, K. (2020). Reclaiming subsidized land: An evaluation of coal gangue interlayers. *Advances in Materials Science and Engineering, 2020*, Article 5740659.

Gong, W., Hui, H., Ma, S., et al. (2025). Preparation of coal gangue-based artificial soil and investigation of the mechanism of aggregate structure formation. *Sustainability, 17*, 3318.

Hu, Y., Han, X., Sun, Z., et al. (2023). Study on the reactivity activation of coal gangue for efficient utilization. *Materials, 16*(18), 6321.

Kamimura, Y., Edagawa, K., & Takeuchi, S. (2013). Experimental evaluation of the Peierls stresses in a variety of crystals and their relation to the crystal structure. *Acta Materialia, 61*(1), 294–309.

Khare, S., Dell'Amico, M., Knight, C., et al. (2013). Selection of materials for high temperature sensible energy storage. *Solar Energy Materials and Solar Cells, 115*, 114–122.

Kocak, B., Fernández, A. I., & Paksoy, H. (2021a). Benchmarking study of demolition wastes with different waste materials as sensible thermal energy storage. *Solar Energy Materials and Solar Cells, 219*, Article 110777.

Kocak, B., Fernández, A. I., & Paksoy, H. (2021b). Characterization of demolition waste powder to be processed as sensible thermal energy storage material. *Solar Energy Materials and Solar Cells, 230*, Article 111283.

Kocak, B., & Paksoy, H. (2020). Performance of laboratory scale packed-bed thermal energy storage using new demolition waste based sensible heat materials for industrial solar applications. *Solar Energy, 211*, 1335–1346.

Koroleva, O. N., Shtenberg, M. V., & Osipov, A. A. (2023). Structural features of K2O–SiO2 melts: Modeling and high-temperature experiments. *Minerals, 13*(1), 94.

Lai, Z., Zhou, H., Zhou, M., et al. (2022). Experimental study on storage performance of packed bed solar thermal energy storage system using sintered ore particles. *Solar Energy Materials and Solar Cells, 238*, Article 111654.
Li, J., & Wang, J. (2019). Comprehensive utilization and environmental risks of coal gangue: A review. *Journal of Cleaner Production, 239*, Article 117946.
Liu, X., Li, H., Lv, L., et al. (2025a). Experimental study on single-unit solid particle packed bed for thermal energy storage of extracted steam from thermal power plant to consume more renewable energy. *Particuology, 97*, 99–116.
Liu, Z., Zhang, F., Zheng, G., et al. (2025b). Recovery of iron from iron tailings by co-pyrolysis with coal gangue: Process optimization and economic evaluation. *Scientific Reports, 16*(1), 2754.
Rahman, M. M., Muttakin, M., Pal, A., et al. (2019). A statistical approach to determine optimal models for IUPAC-classified adsorption isotherms. *Energies, 12*(23), 4565.
Rijimoleng, S., & Gang, H. (2018). DID analysis on the impact of policies on the rural-urban income disparity in resource-dependent regions: A case study of ordos. *International Journal of Economics and Finance, 10*, 191, 191.
Romero, M., Padilla, I., Contreras, M., et al. (2021). Mullite-based ceramics from mining waste: A review. *Minerals, 11*(3), 332.
Shair, J., Li, H., Hu, J., et al. (2021). Power system stability issues, classifications and research prospects in the context of high-penetration of renewables and power electronics. *Renewable and Sustainable Energy Reviews, 145*, Article 111111.
Wang, J., Gu, Y., Yuan, D., et al. (2025). Heat transfer characteristics of $CaO/Ca(OH)_2$ particle fluidization for thermochemical energy storage. *Particuology, 102*, 41–52.
Wang, J., & Guo, X. (2020). Adsorption isotherm models: Classification, physical meaning, application and solving method. *Chemosphere, 258*, Article 127279.
Wang, Z., Tang, Z., Xu, L., et al. (2022a). Thermal properties and thermal cycling stability of graphite/copper composite fabricated by microwave sintering. *Journal of Materials Research and Technology, 20*, 1352–1363.
Wang, B. R., Yang, H. Y., Jin, Z. N., et al. (2022b). Effect of Fe/SiO2 ratio and Fe2O3 on the viscosity and slag structure of copper-smelting slags. *Metals, 12*(1), 24.
Wen, H., Lu, J. H., Xiao, Y., et al. (2015). Temperature dependence of thermal conductivity, diffusion and specific heat capacity for coal and rocks from coalfield. *Thermochimica Acta, 619*, 41–47.
Xiong, Y., He, M., Wu, Y., et al. (2025). A comprehensive review on the utilization of industrial solid waste in thermal energy storage field. *Solar Energy Materials and Solar Cells, 285*, Article 113562.
Xu, B., Liu, Q., Ai, B., et al. (2018). Thermal decomposition of selected coal gangue. *Journal of Thermal Analysis and Calorimetry, 131*, 1413–1422.
Zeng, G., Hou, S., Guo, Q., et al. (2025). Advances in solid particle thermal energy storage: A comprehensive review. *Sustainability, 17*(16), 7244.
Zhang, L., Zhu, D., Marani, A., et al. (2025). Toward sustainable construction: Comprehensive utilization of coal gangue in building materials. *Case Studies in Construction Materials, 23*, Article e04930.
Zhao, Y., Song, J., Liu, M., et al. (2022). Thermo-economic assessments of pumped-thermal electricity storage systems employing sensible heat storage materials. *Renewable Energy, 186*, 431–456.